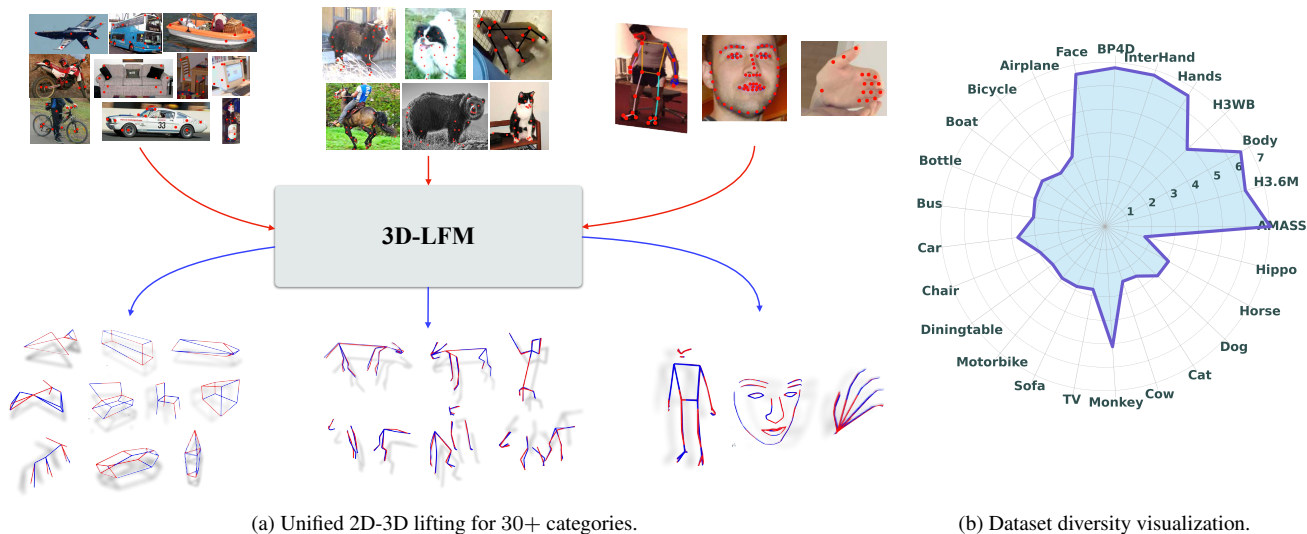


3D-LFM: Lifting Foundation Model

Mosam Dabhi¹ László A. Jeni^{1*} Simon Lucey^{2*}

¹Carnegie Mellon University ²The University of Adelaide

3dlfm.github.io



(a) Unified 2D-3D lifting for 30+ categories.

(b) Dataset diversity visualization.

Figure 1. Overview: (a) This figure shows the 3D-LFM’s ability in lifting 2D landmarks into 3D structures across an array of over 30 diverse categories, from human body parts, to a plethora of animals and everyday common objects. The lower portion shows the actual 3D reconstructions by our model, with red lines representing the ground truth and blue lines showing the 3D-LFM’s predictions. (b) This figure displays the model’s training data distribution on a logarithmic scale, highlighting that in spite of 3D-LFM being trained on imbalanced datasets, it preserves the performance across individual categories.

Abstract

The lifting of 3D structure and camera from 2D landmarks is at the cornerstone of the entire discipline of computer vision. Traditional methods have been confined to specific rigid objects, such as those in Perspective-n-Point (PnP) problems, but deep learning has expanded our capability to reconstruct a wide range of object classes (e.g. C3PDO [18] and PAUL [24]) with resilience to noise, occlusions, and perspective distortions. All these techniques, however, have been limited by the fundamental need to establish correspondences across the 3D training data – significantly limiting their utility to applications where one has an abundance of “in-correspondence” 3D data. Our approach harnesses the inherent permutation equivariance of transformers to manage varying number of points per 3D data instance, withstands occlusions, and generalizes to un-

seen categories. We demonstrate state of the art performance across 2D-3D lifting task benchmarks. Since our approach can be trained across such a broad class of structures we refer to it simply as a 3D Lifting Foundation Model (3D-LFM) — the first of its kind.

1. Introduction

Lifting 2D landmarks from a single-view RGB image into 3D has long posed a complex challenge in the field of computer vision because of the ill-posed nature of the problem. This task is important for a range of applications from augmented reality to robotics, and requires an understanding of non-rigid spatial geometry and accurate object descriptions [2, 11, 25]. Historically, efforts in single-frame 2D-3D lifting have encountered significant hurdles: a reliance on object-specific models, poor scalability, and limited adaptability to diverse and complex object categories. Traditional methods, while advancing in specific domains like human

*Both authors advised equally.

body [14, 16, 31] or hand modeling [3, 6], often fail when faced with the complexities of varying object types or object rigs (skeleton placements).

To facilitate such single-frame 2D-3D lifting, deep learning methods like C3DPO [18] and others [8, 11, 24, 25, 28] have been recently developed. However, these methods are fundamentally limited in that they must have knowledge of the object category and how the 2D landmarks correspond semantically to the 2D/3D data it was trained upon. Further, this represents a drawback, especially when considering their scaling up to dozens or even hundreds of object categories, with varying numbers of landmarks and configurations. This paper marks a departure from such correspondence constraints, introducing the 3D Lifting Foundation Model (3D-LFM), an object-agnostic single frame 2D-3D lifting approach. At its core, the 3D-LFM addresses the limitation of previous models, which is the inability to efficiently handle a wide array of object categories while maintaining high fidelity in 3D keypoint lifting from 2D data. We propose a solution rooted in the concept of permutation equivariance, a property that allows our model to autonomously establish correspondences among diverse sets of input 2D keypoints.

3D-LFM is able to carry out single-frame 2D-3D lifting for 30+ categories using a single model simultaneously, covering everything from human forms [9, 15, 32], face [29], hands [17], and animal species [1, 10, 27], to a plethora of inanimate objects found in everyday scenarios such as cars, furniture, etc. [26]. 3D-LFM is able to achieve 2D-3D lifting performance that matches those of leading methods specifically optimized for individual categories. 3D LFM’s generalizability is further evident in its ability to handle out-of-distribution (OOD) object categories and rigs, which we refer as OOD 2D-3D lifting, where the task is to lift the 2D landmarks to 3D for a category never seen during training. We show such OOD results: (1) for inanimate objects - by holding out an object category within the PASCAL dataset, (2) for animals - by training on common object categories such as dogs and cats found in [27] and reconstructing 3D for unseen and rare species of Cheetahs found in [10] and in-the-wild zoo captures from [5], and (3) by showing rig transfer, *i.e.* training 2D to 3D lifting on a Human3.6M dataset rig [7] and showing similar 2D to 3D lifting performance on previously unseen rigs such as those found in Panoptic studio dataset rig [9] or a COCO dataset rig [13]. 3D-LFM transfers learnings from seen data during training to unseen OOD data during inference. It does so by learning general structural features during the training phase via the proposed permutation equivariance properties and specific design choices that we discuss in the following sections.

Recognizing the important role that geometry plays in 3D reconstruction [4, 5, 11, 18, 24, 25], we integrate Pro-

crustean methods such as Orthographic-N-Point (OnP) or Perspective-N-Point (PnP) to direct the model’s focus on deformable aspects within a canonical frame. This incorporation significantly reduces the computational onus on the model, freeing it from learning redundant rigid rotations and focusing its capabilities on capturing the true geometric essence of objects. Scalability, a critical aspect of our model, is addressed through the use of tokenized positional encoding (TPE), which when combined with graph-based transformer architecture, not only enhances the model’s adaptability across diverse categories but also strengthens its ability to handle multiple categories with different number of keypoints and configurations. Moreover, the use of skeleton information (joint connectivity) within the graph-based transformers via adjacency matrices provides strong clues about joint proximity and inherent connectivity, aiding in the handling of correspondences across varied object categories.

To the best of our knowledge, 3D-LFM is one of the only known work which is a unified model capable of doing 2D-3D lifting for 30+ (and potentially even more) categories simultaneously. Its ability to perform unified learning across a vast spectrum of object categories without specific object information and its handling of OOD scenarios highlight its potential as one of the first models capable of serving as a 2D-3D lifting foundation model.

The contributions of this paper are threefold:

1. We propose a Procrustean transformer that is able to focus solely on learning the deformable aspects of objects within a single canonical frame whilst preserving permutation equivariance across 2D landmarks.
2. The integration of tokenized positional encoding within the transformer, to enhance our approach’s scalability and its capacity to handle diverse and imbalanced datasets.
3. We demonstrate that 3D-LFM surpasses state-of-the-art methods in categories like humans, hands, and faces (benchmark in [32]). Additionally, it shows robust generalization by handling previously unseen objects and configurations, including animals ([5, 10]), inanimate objects ([26]), and novel object arrangements (rig transfer in [9])

In subsequent sections, we explore the design and methodology of our proposed 3D-LFM architecture, including detailed ablation experiments and comparative analyses. Throughout this paper, ‘keypoints,’ ‘landmarks,’ and ‘joints’ are used interchangeably, referring to specific, identifiable points or locations on an object or figure that are crucial for understanding its structure and geometry.

2. Related works

The field of 2D-3D lifting has evolved substantially from classic works such as the Perspective-n-Point (PnP) al-

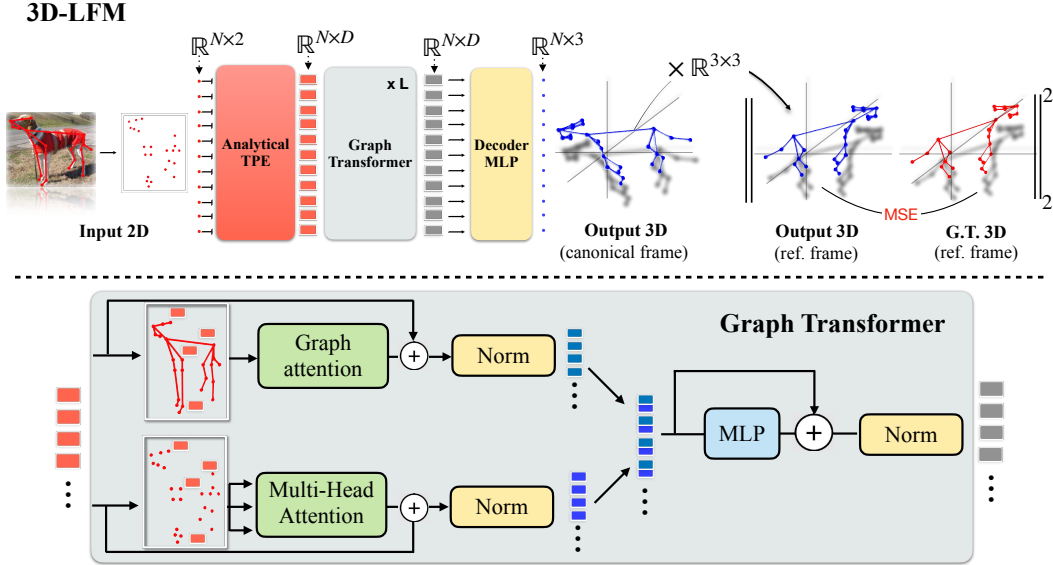


Figure 2. **Overview of the 3D Lifting Foundation Model (3D-LFM) architecture:** The process begins with the input 2D keypoints undergoing Token Positional Encoding (TPE) before being processed by a series of Graph-based Transformer layers. The resulting features are then decoded through an MLP into a canonical 3D shape. This shape is aligned to the ground truth (G.T. 3D) in the reference frame using a Procrustean method, with the Mean Squared Error (MSE) loss computed to guide the learning. The architecture captures both local and global contextual information, focusing on deformable structures while minimizing computational complexity.

gorithm [12]. In these early works, the algorithm was given a set of 2D landmarks and some 3D supervision – namely the known 3D rigid object. The field has since witnessed a paradigm shift with the introduction of deep learning methodologies, led by methods such as C3DPDO [18], PAUL [24], and Deep NRSfM [11], along with recent transformer-based innovations like NRSfMFormer [8]. In these approaches one does not need knowledge of the specific 3D object, instead it can get away with just the 2D landmarks and correspondences to an ensemble of 2D/3D data from the object category to be lifted. However, despite their recent success, all these methods still require that the 2D/3D data be in semantic correspondence. That is the index to a specific landmark has the same semantic meaning across all instances (e.g. chair leg). In practice, this is quite limiting at run-time, as one needs intimate knowledge of the object category, and rig in order to apply any of these current methods. Further, this dramatically limits the ability of these methods to leverage cross-object and cross-rig datasets, prohibiting the construction of a truly generalizable 2D to 3D foundation lifting model – a topic of central focus in this paper.

Recent literature in pose estimation, loosely connected to NRSfM but often more specialized towards human and animal body part, has also seen remarkable progress. Models such as Jointformer [14] and SimpleBaseline [16] have refined the single-frame 2D-3D lifting process, while gen-

erative approaches like MotionCLIP [19] and Human Motion Diffusion Model [20] have laid the groundwork for 3D generative motion-based foundation models. These approaches, however, are even more limiting than C3DPDO, PAUL, etc. in that they are intimately wedded to the object class and are not easily extendable to an arbitrary objects class.

3. Approach

Given a set of 2D keypoints representing the projection of an object’s joints in an image, we denote the keypoints matrix as $\mathbf{W} \in \mathbb{R}^{N \times 2}$, where N is the predetermined maximum number of joints considered across all object categories. For objects with joints count less than N , we introduce a masking mechanism that utilizes a binary mask matrix $\mathbf{M} \in \{0, 1\}^N$, where each element m_i of \mathbf{M} is defined as:

$$m_i = \begin{cases} 1 & \text{if joint } i \text{ is present} \\ 0 & \text{otherwise} \end{cases} \quad (1)$$

The 3D lifting function $f : \mathbb{R}^{N \times 2} \rightarrow \mathbb{R}^{N \times 3}$ maps the 2D keypoints to their corresponding 3D structure while compensating for the orthographic projection:

$$\mathbf{S} = f(\mathbf{W}) = \mathbf{W}\mathbf{P}^\top + \mathbf{b} \quad (2)$$

where $\mathbf{P} \in \mathbb{R}^{3 \times 2}$ is the orthographic projection matrix

and $\mathbf{b} \in \mathbb{R}^{N \times 3}$ is a bias term that aligns the centroids of 2D and 3D keypoints.

Permutation Equivariance: To ensure scalability and adaptability across a diverse set of objects, we leverage the property of permutation equivariance inherent in transformer architectures. Permutation equivariance allows the model to process input keypoints \mathbf{W} regardless of their order, a critical feature for handling objects with varying joint configurations:

$$f(\mathcal{P}\mathbf{W}) = \mathcal{P}f(\mathbf{W})$$

where \mathcal{P} is a permutation matrix that reorders the keypoints.

Handling Missing Data: To address the challenge of missing data, we refer to the Deep NRSfM++ [25] work and use a masking mechanism to accommodate for occlusions or absences of keypoints. Our binary mask matrix $\mathbf{M} \in \{0, 1\}^N$ is applied in such a way that it not only pads the input data to a consistent size but also masks out missing or occluded points: $\mathbf{W}_m = \mathbf{W} \odot \mathbf{M}$, where \odot denotes element-wise multiplication. To remove the effects of translation and ensure that our TPE features are generalizable, we zero-center the data by subtracting the mean of the visible keypoints:

$$\mathbf{W}_c = \mathbf{W}_m - \text{mean}(\mathbf{W}_m) \quad (3)$$

We scale the zero-centered data to the range $[-1, 1]$ while preserving the aspect ratio to maintain the geometric integrity of the keypoints. For more details on handling missing data in the presence of perspective effects, we refer the reader to Deep NRSfM++ [25].

Token Positional Encoding: replaces the traditional Correspondence Positional Encoding (CPE) or Joint Embedding which encodes the semantic correspondence information (as used in works such as like [14, 31]) with a mechanism that does not require explicit correspondence or semantic information. Owing to the success of per-point positional embedding, particularly random Fourier features [30] in handling OOD data, we compute Token Positional Encoding (TPE) using analytical Random Fourier features (RFF) as follows:

$$\text{TPE}(\mathbf{W}_c) = \sqrt{\frac{2}{D}} \left[\sin(\mathbf{W}_c \boldsymbol{\omega} + b); \cos(\mathbf{W}_c \boldsymbol{\omega} + b) \right] \quad (4)$$

where D is the dimensionality of the Fourier feature space, $\boldsymbol{\omega} \in \mathbb{R}^{2 \times \frac{D}{2}}$ and $b \in \mathbb{R}^{\frac{D}{2}}$ are parameters sampled from a normal distribution, scaled appropriately. These parameters are sampled once and kept fixed, as per the RFF methodology. The output of this transformation $\text{TPE}(\mathbf{W}_c)$ is then fed into the Graph Transformer network as \mathbf{X}^ℓ where ℓ indicates the layer number (0 in the above case). This set of features is now ready for processing inside the graph-

based transformer layers without the need for correspondence among the input keypoints. The TPE retains the permutation equivariance property while implicitly encoding the relative positions of the keypoints.

3.1. Graph-based Transformer Architecture

Our Graph-based Transformer architecture utilizes a hybrid approach to feature aggregation by combining graph-based local attention [22](L) with global self-attention mechanisms [21](G) within a single layer (shown as grey block in Fig. 2). This layer is replicated L times, providing a sequential refinement of the feature representation across the network’s depth.

Hybrid Feature Aggregation: For each layer ℓ , with ℓ ranging from 0 to L , the feature matrix $\mathbf{X}^{(\ell)} \in \mathbb{R}^{N \times D}$ is augmented through simultaneous local and global processing:

$$\begin{aligned} \mathbf{L}^{(\ell)} &= \text{GA}(\mathbf{X}^{(\ell)}, \mathbf{A}), \\ \mathbf{G}^{(\ell)} &= \text{MHSA}(\mathbf{X}^{(\ell)}) \end{aligned} \quad (5)$$

Local and global features are concatenated to form a unified representation $\mathbf{U}^{(\ell)}$:

$$\mathbf{U}^{(\ell)} = \text{concat}(\mathbf{L}^{(\ell)}, \mathbf{G}^{(\ell)}) \quad (6)$$

Following the concatenation, each layer applies a normalization(LN) and a multilayer perceptron (MLP). The MLP employs a Gaussian Error Linear Unit (GeLU) as the nonlinearity function to enhance the model’s expressive power

$$\begin{aligned} \mathbf{X}'^{(\ell)} &= \text{LN}(\mathbf{U}^{(\ell)}) + \mathbf{U}^{(\ell)}, \\ \mathbf{X}^{(\ell+1)} &= \text{LN}(\text{MLP_GeLU}(\mathbf{X}'^{(\ell)})) + \mathbf{X}'^{(\ell)} \end{aligned} \quad (7)$$

Here, GA represents Graph Attention, MHSA denotes Multi-Head Self-Attention, and MLP_GeLU indicates our MLP with GeLU nonlinearity. This architecture is designed to learn complex patterns by considering both the local neighborhood connectivity of input 2D and the global data context of input 2D, which is important for robust 2D to 3D structure lifting.

3.2. Procrustean Alignment

The final operation in our pipeline decodes the latent feature representation $\mathbf{X}^{(L)}$ into the predicted canonical structure \mathbf{S}_c via a GeLU-activated MLP:

$$\mathbf{S}_c = \text{MLP}_{\text{shape_decoder}}(\mathbf{X}^{(L)})$$

Subsequently, we align \mathbf{S}_c with the ground truth \mathbf{S}_r , via a Procrustean alignment method that optimizes for the rotation matrix \mathbf{R} . The alignment is formalized as a minimization problem:

$$\underset{\mathbf{R}}{\text{minimize}} \quad \|\mathbf{M} \odot (\mathbf{S}_r - \mathbf{S}_c \mathbf{R})\|_F^2$$

where \mathbf{M} is a binary mask applied element-wise, and $\|\cdot\|_F$ denotes the Frobenius norm. The optimal \mathbf{R} is obtained via SVD, which ensures the orthonormality constraint of the rotation matrix:

$$\begin{aligned} \mathbf{U}, \mathbf{\Sigma}, \mathbf{V}^\top &= \text{SVD}((\mathbf{M} \odot \mathbf{S}_c)^\top \mathbf{S}_r) \\ \mathbf{R} &= \mathbf{U}\mathbf{V}^\top \end{aligned}$$

The predicted shape is then scaled relative to the reference shape \mathbf{S}_r , resulting in a scale factor γ , which yields the final predicted shape \mathbf{S}_p :

$$\mathbf{S}_p = \gamma \cdot (\mathbf{S}_c \mathbf{R})$$

This Procrustean alignment step is crucial for directing the model’s focus on learning non-rigid shape deformations over rigid body dynamics, thus significantly enhancing the model’s ability to capture the true geometric essence of objects by just focusing on core deformable (non-rigid) aspects. The effectiveness of this approach is confirmed by faster convergence and reduced error rates in our experiments, as detailed in Fig. 6. These findings align with the findings presented in PAUL [24].

3.3. Loss Function

The optimization of our model relies on the Mean Squared Error (MSE) loss, which calculates the difference between predicted 3D points \mathbf{S}_p and the ground truth \mathbf{S}_r :

$$\mathcal{L}_{\text{MSE}} = \frac{1}{N} \sum_{i=1}^N \|\mathbf{s}_p^{(i)} - \mathbf{s}_r^{(i)}\|^2 \quad (8)$$

Minimizing this loss across N points ensures the model’s ability in reconstructing accurate 3D shapes from input 2D landmarks. This minimization effectively calibrates the shape decoder and the Procrustean alignment to focus on the essential non-rigid characteristics of the objects, helping the accuracy of the 2D to 3D lifting process.

4. Results and Comparative Analysis

Our evaluation shows the 3D Lifting Foundation Model (3D-LFM)’s capability in single-frame 2D-3D lifting across diverse object categories without object-specific data in Sec. 4.1. Following that, Sec. 4.2 highlights 3D-LFM’s performance over specialized methods, especially in whole-body benchmarks (referenced in [32]), showcasing adaptability across varied categories like the human body, face, and hands (Fig.4). Additionally, Section 4.3 shows 3D-LFM’s capability in 2D-3D lifting across 30 categories using a single unified model, enhancing category-specific performance and achieving out-of-distribution (OOD) generalization for unseen object configurations during training.

Concluding, ablation studies in Section 4.4 validates our proposed OnP approach, token positional encoding, and the hybrid-attention mechanism in the transformer model, confirming their role in 3D-LFM’s effectiveness in both single and multiple-object scenarios.

4.1. Multi-Object 3D Reconstruction

Experiment Rationale: The 3D-LFM is designed to process diverse sets of 2D keypoints and lift them into 3D across multiple object categories without relying on category-specific information. Its key strength lies in permutation equivariance, which maintains consistent performance regardless of keypoint order—this is critical when handling multiple objects with different numbers of keypoints. Unlike methods that depend on fixed-dimension arrays to manage object information, our model adapts flexibly to the data at hand. It has been evaluated against non-rigid structure-from-motion approaches [11, 18, 24, 25] that require object-specific inputs, showing its ability to handle diverse categories. For a comprehensive benchmark, we utilize the PASCAL3D+ dataset [26], following C3DPO’s [18] methodology, to include a variety of object categories.

Performance: We benchmark our 3D-LFM against C3DPO [18], a leading method in the NRSfM domain, to evaluate its performance in multi-object 2D to 3D lifting tasks, with 3D supervision. While other recent methods [11, 24, 25, 28] also require object-specific details, C3DPO’s approach to multiple object categories makes it a suitable comparison for our model. Initially, we replicate conditions where object-specific information is provided, resulting in comparable performance between 3D-LFM and C3DPO, evident in Fig. 3. This stage involves using the Mean-per-joint-position-error (MPJPE) to measure 2D-3D lifting accuracy, with C3DPO’s training setup including an MN dimensional array for object details where M represents number of objects with N being maximum number of keypoints, and our model is trained separately on each object to avoid providing object-specific information.

The 3D-LFM’s strength is most apparent when object-specific data is withheld. Unlike C3DPO, which experiences performance drops without object details, our model sustains a lower MPJPE, even when trained collectively across categories using only an N dimensional array. The results (Fig.3 and Tab.1) highlight 3D-LFM’s robustness and superior adaptability, outperforming single-category training and demonstrating its potential as a generalized 2D to 3D lifting solution.

4.2. Benchmark: Object-Specific Models

We benchmark our 3D Lifting Foundation Model (3D-LFM) against leading specialized methods for human body, face, and hands categories. Our model outperforms these specialized methods, showcasing its broad utility without

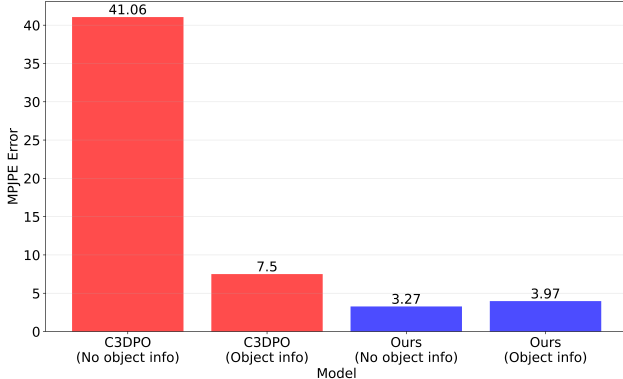


Figure 3. This figure shows the MPJPE for 3D-LFM and C3DPO using the PASCAL3D+ dataset, comparing performance with and without object-specific information. Both methods perform comparably when object-specific information is provided. However, absent this data, C3DPO’s error increases markedly, whereas 3D-LFM’s remains low, showcasing its robustness and adaptability across varied object categories without relying on object-specific information.

Table 1. Quantitative Comparison of Multi-Object 2D-3D Lifting Performance

Method	Object-specific	MPJPE (avg)
C3DPO [18]	Yes	7.5
3D-LFM (Ours)	Yes	3.97
C3DPO [18]	No	41.08
3D-LFM (Ours)	No	3.27

the need for object-specific tailoring, highlighting the versatility of its object-agnostic architecture. For our evaluation, we utilize the H3WB dataset [32], a recent benchmark for diverse whole-body pose estimation tasks. This dataset is especially valuable for its inclusion of multiple object categories and for providing a comparative baseline against methods like Jointformer [14], SimpleBaseline [16], and CanonPose [23]. We followed the H3WB’s recommended 5-fold cross-validation and engaged with the benchmark’s authors to obtain results on the hidden test set. Our reported metrics in Fig. 4 and Table 2 include PA-MPJPE and MPJPE, with the test set performance numbers provided directly by the H3WB team, ensuring that our superior results are verified by an independent third-party.

Performance: Our 3D-LFM demonstrates a notable enhancement in accuracy over baseline methods, as outlined in the referenced figure and table. It excels across all categories, including whole-body, body, face, and hands, as shown in Fig. 4 and detailed in Tab. 2. With a lean architecture of only 5 million parameters—significantly fewer than comparative baseline approaches, our model achieves

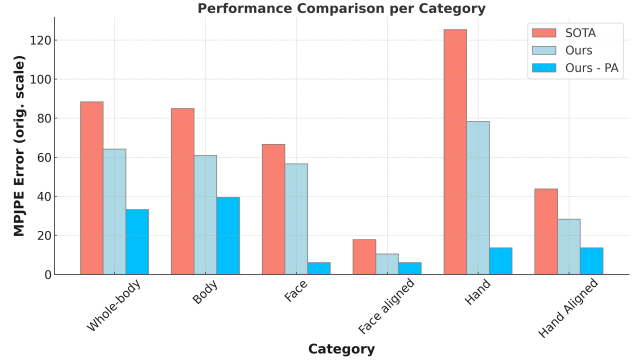


Figure 4. **Performance Comparison on H3WB Benchmark:** This chart contrasts MPJPE errors for whole-body, body, face, aligned face, hand, and aligned hand categories within the H3WB benchmark [32]. Our models, with and without Procrustes Alignment (Ours-PA), outperform current state-of-the-art (SOTA) methods, validating our approach’s proficiency in 2D to 3D lifting tasks.

Table 2. Performance evaluation of 3D pose estimation models on H3WB and validation datasets showing MPJPE in millimeters. Our method demonstrates leading accuracy across multiple object categories without the need for object-specific designs.

Method	Whole-body	Body	Face/Aligned	Hand/Aligned
SimpleBaseline	125.4	125.7	115.9 / 24.6	140.7 / 42.5
CanonPose w/3D sv.	117.7	117.5	112.0 / 17.9	126.9 / 38.3
Large SimpleBaseline	112.3	112.6	110.6 / 14.6	114.8 / 31.7
Jointformer (extra data)	81.5	78	60.4 / 16.2	117.6 / 38.8
Jointformer	88.3	84.9	66.5 / 17.8	125.3 / 43.7
Ours	64.13	60.83	56.55 / 10.44	78.21 / 28.22
Ours - PA	33.13	39.36	6.02	13.56

rapid convergence and can be trained efficiently on a single NVIDIA A100 GPU within hours, emphasizing our model’s efficiency and scalability evident by robust performance across varied object categories.

The results affirm 3D-LFM as a versatile and potent foundational model for diverse 2D to 3D lifting tasks, outpacing specialized category-specific models. These findings, showcased in Fig. 4, validate our model’s ability to leverage inter-category learning, potentially paving the way for broader applications across an expanded range of object categories.

4.3. Towards foundation model

In this section, we demonstrate the 3D Lifting Foundation Model (3D-LFM) as a versatile foundation for diverse 2D-3D lifting scenarios. Our model is capable of handling various object categories and navigating data imbalance challenges. In this subsection, we explore the 3D-LFM’s scalability and its potential for combined dataset training in Sec. 4.3.1, its proficiency in generalizing to unseen object categories and its adaptability in transferring rig configura-

tions in Sec. 4.3.2. These studies validate the 3D-LFM’s role as a foundation model, capable at leveraging diverse data without requiring specific configurations, thus simplifying the 3D lifting process for varied joint setups.

We show 3D-LFM’s capability of handling 2D-3D lifting for 30+ object categories within the single model, confirming the model’s capability to manage imbalanced datasets representative of real-world scenarios as shown in Fig. 1. With a comprehensive range of human, hand, face, inanimate objects, and animal datasets, the 3D-LFM is proven to be adaptable, not necessitating category-specific adjustments. The subsequent subsections will dissect these attributes further, discussing the 3D-LFM’s foundational potential in the 3D lifting domain.

4.3.1 Combined Dataset Training

This study evaluates the 3D-LFM’s performance on isolated datasets against its performance on a comprehensive combined dataset. Initially, the model was trained separately on animal-based supercategory datasets—specifically **OpenMonkey**[1] and **Animals3D**[27]. Subsequently, it was trained on a merged dataset encompassing a broad spectrum of object categories, including **Human Body-Based** datasets like AMASS and Human 3.6 [7], **Hands-Based** datasets such as PanOptic Hands [9], **Face-Based** datasets like BP4D+[29], and various **Inanimate Objects** from the PASCAL3D+ dataset[26], along with the previously mentioned animal datasets. Isolated training resulted in an average MPJPE of 21.22 mm, while the integrated training method notably reduced the MPJPE to 12.5 mm on the same animal supercategory validation split. This significant improvement confirms the 3D-LFM’s potential as a pretraining framework and underscores its capacity to adapt to and generalize from diverse and extensive data collections.

4.3.2 OOD generalization and rig-transfer:

We evaluated the 3D-LFM’s generalization ability on object categories and rig configurations unseen during training. The model’s proficiency is demonstrated through its accurate 3D reconstructions of the “Cheetah” category from the Acinonet dataset [10]—distinct from the commonly seen species in the Animal3D dataset [27]. A similar generalization is observed when the model, trained without the “Train” category from PASCAL3D+[26], accurately reconstructs its 3D structure. These findings confirm the model’s robust out-of-distribution (OOD) generalization capability, as qualitatively illustrated in Fig. 5.

Additionally, the 3D-LFM showcased its capability in transferring rig configurations between datasets. For example, training on a 17-joint Human3.6M dataset [7] and testing on a 15-joint Panoptic Studio dataset [9] led to accurate 3D reconstructions, despite the disparity in joint

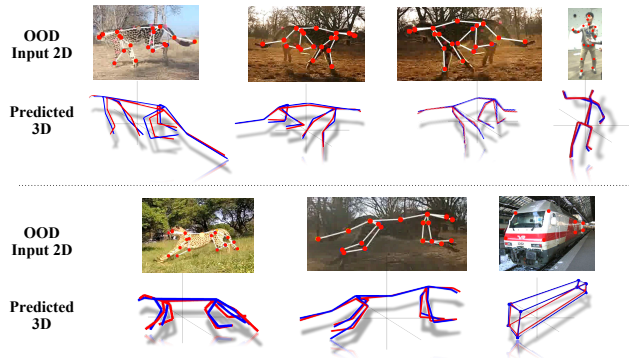


Figure 5. This figure illustrates 3D-LFM’s proficiency in OOD 2D-3D lifting, effectively handling new, unseen categories from Acinonet [10] PASCAL3D+ [26] with varying joint arrangements, demonstrating its strong generalization capabilities.

numbers and arrangements. These results emphasize the foundational model’s adaptability, critical for processing diverse human data sets with varying rig setups. For a more thorough validation, we direct readers to the ablation section, where extensive qualitative visualizations in Fig. 7 and quantitative reports in Sec. 4.4.3 further substantiate the 3D-LFM’s OOD generalization and rig transfer efficacy.

4.4. Ablation

We conduct ablation studies to dissect the 3D-LFM’s design choices and their respective contributions. The experiments in Sec. 4.4.1 and Sec. 4.4.2 are carried out on the Human3.6M benchmark [7] and a mixture of Animal3D [27], Human3.6M, and face datasets [9, 29] are used in Sec. 4.4.3 to emphasize the scalability and OOD generalization properties of TPE.

4.4.1 Procrustean Transformation

The Procrustean approach within 3D-LFM refines learning to the deformable components of objects. Utilizing an OnP solution described in Sec. 3.2, the model focuses on learning deformable shapes in the canonical space and ignoring rigid transformations. The faster convergence and reduced MPJPE error, evident by the gap between blue and orange lines in Fig. 6 (a) validates the benefits of Procrustean transformation, confirming its relevance in the architecture.

4.4.2 Local-Global vs. Hybrid Attention

On the same validation split, our analysis indicates that merging local (GA) and global attention (MHSA) leads to the best performance. Isolating either attention mechanism does not match the performance of their combined use, as shown by the green and red lines in as shown in Fig. 6 (a). The combination of GA with MHSA, especially when aligned with OnP, delivers best results and faster convergence. These findings from our ablation studies validate the

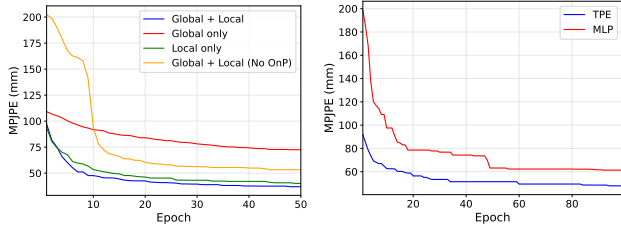


Figure 6. (a) Comparing attention strategies in 3D-LFM. The combined local-global approach with OnP alignment surpasses other configurations in MPJPE reduction over 100 epochs on the Human3.6M validation split. (b) rapid convergence and efficiency of the TPE approach compared to the learnable MLP

architectural decisions behind 3D-LFM.

Our hybrid attention mechanism, which fuses connectivity-aware local graph attention (GA) with the broader scope of global multi-head self-attention (MHSA)—emerges as a more optimal strategy. Sole reliance on either GA or MHSA results in suboptimal performance as evidenced by green and red lines as compared to blue line in Fig. 6 (a). This hybrid attention, paired with Procrustes (OnP) alignment, not only minimizes MPJPE error but also makes model convergence faster, reinforcing the architectural decisions underlying the 3D-LFM.

4.4.3 Tokenized Positional Encoding:

This ablation study covers the impact of Tokenized Positional Encoding (TPE) in 3D-LFM, which leverages analytical Random Fourier Features for positional information, retaining the permutation equivariance and scalability essential for a foundational model.

Data imbalance study: Our experiments on the Animal3D dataset [27], with a focus on the underrepresented hippo supercategory, reveal TPE’s efficacy in dealing with imbalanced dataset. With a nominal model size of 128 dimensions, TPE improved MPJPE performance by **3.27%** over the learnable MLP approach, and this performance kept improving as we kept increasing the model size from 128 to 512 and finally to 1024 - where the performance improvement kept improving from **3.27%** to **12.28%**, and finally to **22.02%** - highlighting its capability to handle data imbalance with varying model sizes. More importantly, for all these trials one important thing we noticed is the statistically significant faster convergence shown by TPE over learnable MLP approach as evident in Fig. 6 (b).

Rig Transfer Generalization: Rig transfer experiments further solidify TPE’s efficacy, with a **12%** improvement when transferring from a 17-joint [7] to a 15-joint rig [9] and an improvement of **23.29%** when we trained on 15-joint rig and tested on 17-joint rig. Training on a 52-joint facial rig from [9] and testing on an 83-joint from [29] yielded

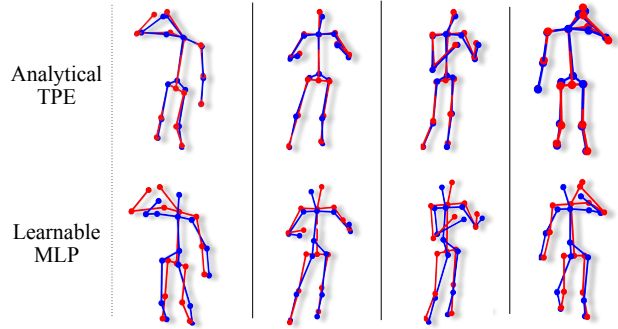


Figure 7. The qualitative improvement in rig transfer using analytical TPE versus learnable MLP projection. This visualization reinforces the necessity of TPE in handling OOD data such as different rigs, unseen during training.

a **52.3%** improvement over the MLP baseline, validating TPE’s robustness in complex OOD scenarios. Fig. 7 qualitatively shows TPE’s performance, where the our model with TPE is able to generalize to unseen joint configurations. This ablation section touches upon both quantitative and visual studies of TPE and conveys that TPE is a pivotal component for scalable 2D-3D lifting task.

5. Discussion and Conclusion

The proposed 3D-LFM marks a significant leap in 2D-3D lifting, showcasing scalability and adaptability, addressing data imbalance, and generalizing to new data categories. Its cross-category knowledge transfer and rare shape variation handling requires further investigation to enhance robustness. 3D-LFM’s efficiency is demonstrated by achieving results comparable to leading methods on [32] benchmark as well as its proficiency in out-of-distribution (OOD) scenarios on limited computational resources. For training duration and computational details, please refer to the supplementary materials. This work not only pushes the boundaries of current 2D-3D lifting, but also establishes a scalable framework for future 3D pose estimation and 3D reconstruction models. In summary, the 3D-LFM creates a flexible, universally applicable model for 3D reconstruction from 2D data, paving the way for diverse applications that requires accurate 3D reconstructions from 2D inputs.

Acknowledgement: We extend our gratitude to Ian R. Fasel, Tim Clifford, Javier Movellan, Matthias Hernandez, Matthias Schroeder, and Akshay Subramanya of Apple for their insightful discussions.

Supplementary Material

I. Training Details

The 3D Lifting Foundation Model (3D-LFM), as detailed in Sec. 4.3.1 was trained across more than 30 diverse categories on a single NVIDIA A100 GPU. This dataset consisted of over 18 million samples, with data heavily imbalanced as shown in Fig. 1. This training setup highlights the model’s practicality, with mixed datasets having imbalance within them. 3D LFM’s transformer block, shown in lower half of Fig. 2 consists of 4 layers, with hidden dimensions (post TPE dimension) ranging from 64 to 512 and head counts between 4 and 8. These parameters were adjusted based on the dataset scale in various experiments of Sec. 4. GeLU activations were employed for non-linearity in the feedforward layers. The training process was guided by a ReduceLROnPlateau scheduler with a starting learning rate of 0.001 and a patience of 20 epochs. An early stopping mechanism was implemented, halting training if no improvement in MPJPE was noted for 30 epochs, ensuring efficient and optimal performance. This training approach enabled 3D-LFM to surpass leading methods in 3D lifting task proposed by H3WB benchmark [32].

Experimentation in Section 4.2: For the benchmark experiment of H3WB [32], we adopted a 5-fold cross-validation as directed by the benchmark authors. We trained two model variants: one with OnP solution (predicting shapes, S_c in canonical frame) and one without the OnP solution (predicting shapes directly in the reference frame, S_p). We aligned the canonical frame predictions from the OnP-based model to those from the non-OnP based model, which ensured that the submitted 3D reconstructions have the rotation and scales adjusted to the predicted reference frame.

II. Interactive Visualization with 3D-LFM

The `3d_lfm_visualization.ipynb` notebook provided on our project page provides an in-depth interactive exploration of the 3D-LFM’s model predictions – 3D structures from input 2D landmarks. This interactive notebook shows the model’s adaptability across standard validation datasets (shown in Fig. 1) and its adaptability to challenging Out-Of-Distribution (OOD) scenarios, particularly from in-the-wild captures provided by the Acinonet datasets [10] and MBW datasets [5].

II.1. Key Features

Category Selection: Enables selection from diverse object categories, including standard and OOD. **Data Management:** Automates the loading and visualization of 2D inputs, 3D ground truth, and predictions. **Frame Exploration:** Facilitates detailed visualization of specific frames

with the option to overlay 2D input data on images and viewing its corresponding 3D predictions simultaneously.

II.2. Usage and examples

To use the notebook, simply select an object category and frame number (automated within). It will display the model’s 3D and 2D predictions, alongside available ground truth data. For OOD categories, there’s an option to include pseudo ground truth labels, offering a deeper insight into the model’s performance in diverse scenarios.

As shown in Fig. 8, the 3D-LFM handles complex OOD data, generating predictions in-the-wild with reasonable accuracy. Unlike traditional approaches requiring extensive bootstrapping to generate labels for tail-end distribution categories, our 3D-LFM generates 3D predictions in a single inference step, emphasizing its foundation model capabilities. These include in-the-wild reconstructions of various wildlife captured in-the-wild, as showcased in Fig. 8. This figure, alongside additional visualizations within the notebook shows that 3D-LFM is capable of handling multiple categories within a single unified model. It particularly handles OOD scenarios reasonably well – providing accurate 2D-3D lifting performance on in-the-wild captures from datasets like Acinonet [10] and MBW [5]. These findings confirm the 3D-LFM’s ability to utilize its foundational attributes for accurate 2D-3D lifting, even across previously unseen categories.

III. Limitations

Category Misinterpretation: The 3D-LFM exhibits remarkable performance generalizing across object categories. However, it can encounter difficulties when extreme perspective distortions cause 2D inputs to mimic the appearance of different categories. For example, in the case of a tiger viewed from an atypical angle, the model’s output may resemble the structure of a primate due to similar 2D keypoint configurations induced by perspective effects, as shown in Fig. 9 (c). This confusion stems from the model’s reliance on the geometric arrangement of keypoints, which can be deceptive under extreme perspectives.

Depth Ambiguity: Another challenge arises from the inherent depth ambiguity in single-frame 2D to 3D lifting. The model can misinterpret the spatial arrangement of limbs, as evident by Fig. 9 (a), where a monkey’s leg appears to extend backward rather than forward. Similarly, Fig. 9 (b) displays an instance where the model perceives the monkey’s head orientation incorrectly. Such depth ambiguities highlight the need for more sophisticated depth cues in single-view 3D reconstruction.

We propose integrating appearance cues, such as those

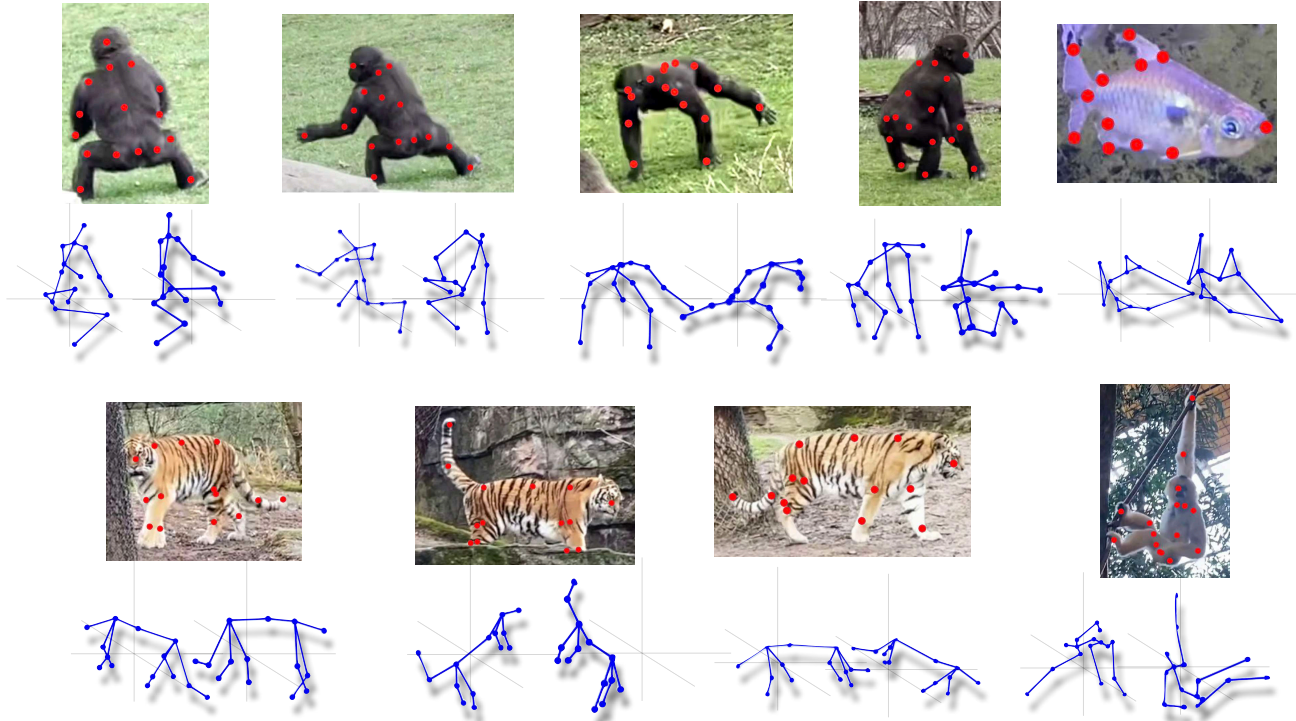


Figure 8. **Example OOD inferences by 3D-LFM on MBW dataset** [5]: The red dots overlaying the images indicate the input 2D keypoints, while the blue stick figures below each image shows the predicted 3D structure viewed from two distinct camera viewing angles. Accompanying video results further illustrate these predictions with a dynamic 360-degree camera animation, providing a detailed view of the model’s performance.

provided by DINOv2 features, to enhance depth perception and category differentiation. This would provide additional context to the geometric data, aiding in resolving ambiguities, as demonstrated by the OOD examples in Fig. 9, derived from challenging in-the-wild captures [5]. This integration aims to improve the fidelity of 3D reconstructions in scenarios with complex visual information.

References

- [1] Praneet C Bala, Benjamin R Eisenreich, Seng Bum Michael Yoo, Benjamin Y Hayden, Hyun Soo Park, and Jan Zimmermann. Openmonkeystudio: Automated markerless pose estimation in freely moving macaques. *BioRxiv*, pages 2020–01, 2020. 2, 7
- [2] Christoph Bregler, Aaron Hertzmann, and Henning Biermann. Recovering non-rigid 3d shape from image streams. In *Proceedings IEEE Conference on Computer Vision and Pattern Recognition. CVPR 2000 (Cat. No. PR00662)*, pages 690–696. IEEE, 2000. 1
- [3] Zheng Chen and Yi Sun. Joint-wise 2d to 3d lifting for hand pose estimation from a single rgb image. *Applied Intelligence*, 53(6):6421–6431, 2023. 2
- [4] Mosam Dabhi, Chaoyang Wang, Kunal Saluja, László A Jeni, Ian Fasel, and Simon Lucey. High fidelity 3d reconstructions with limited physical views. In *2021 International*

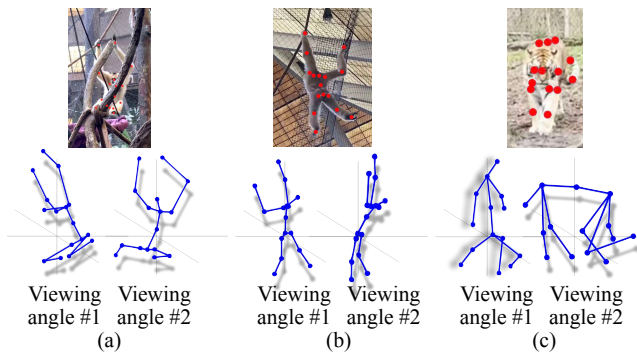


Figure 9. **Challenges in Perspective and Depth Perception:** (a) Incorrect leg orientation due to depth ambiguity in monkey capture. (b) Misinterpreted head position in a second monkey example. (c) A tiger’s keypoints distorted by perspective, leading to primate-like 3D predictions.”

Conference on 3D Vision (3DV), pages 1301–1311. IEEE, 2021. 2

- [5] Mosam Dabhi, Chaoyang Wang, Tim Clifford, László Jeni, Ian Fasel, and Simon Lucey. Mbw: Multi-view bootstrapping in the wild. *Advances in Neural Information Processing Systems*, 35:3039–3051, 2022. 2, 9, 10

- [6] Liuhaog Ge, Zhou Ren, Yuncheng Li, Zehao Xue, Yingying Wang, Jianfei Cai, and Junsong Yuan. 3d hand shape and pose estimation from a single rgb image. In *Proceedings of the IEEE/CVF Conference on Computer Vision and Pattern Recognition*, pages 10833–10842, 2019. [2](#)
- [7] Catalin Ionescu, Dragos Papava, Vlad Olaru, and Cristian Sminchisescu. Human3.6m: Large scale datasets and predictive methods for 3d human sensing in natural environments. *IEEE transactions on pattern analysis and machine intelligence*, 36(7):1325–1339, 2013. [2](#), [7](#), [8](#)
- [8] Haorui Ji, Hui Deng, Yuchao Dai, and Hongdong Li. Unsupervised 3d pose estimation with non-rigid structure-from-motion modeling. *arXiv preprint arXiv:2308.10705*, 2023. [2](#), [3](#)
- [9] Hanbyul Joo, Hao Liu, Lei Tan, Lin Gui, Bart Nabbe, Iain Matthews, Takeo Kanade, Shohei Nobuhara, and Yaser Sheikh. Panoptic studio: A massively multiview system for social motion capture. In *Proceedings of the IEEE International Conference on Computer Vision*, pages 3334–3342, 2015. [2](#), [7](#), [8](#)
- [10] Daniel Joska, Liam Clark, Naoya Muramatsu, Ricardo Jericevich, Fred Nicolls, Alexander Mathis, Mackenzie W Mathis, and Amir Patel. Acinonet: a 3d pose estimation dataset and baseline models for cheetahs in the wild. In *2021 IEEE international conference on robotics and automation (ICRA)*, pages 13901–13908. IEEE, 2021. [2](#), [7](#), [9](#)
- [11] Chen Kong and Simon Lucey. Deep non-rigid structure from motion. In *Proceedings of the IEEE/CVF International Conference on Computer Vision*, pages 1558–1567, 2019. [1](#), [2](#), [3](#), [5](#)
- [12] Vincent Lepetit, Francesc Moreno-Noguer, and Pascal Fua. Ep n p: An accurate o (n) solution to the p n p problem. *International journal of computer vision*, 81:155–166, 2009. [3](#)
- [13] Tsung-Yi Lin, Michael Maire, Serge Belongie, James Hays, Pietro Perona, Deva Ramanan, Piotr Dollár, and C Lawrence Zitnick. Microsoft coco: Common objects in context. In *Computer Vision—ECCV 2014: 13th European Conference, Zurich, Switzerland, September 6–12, 2014, Proceedings, Part V 13*, pages 740–755. Springer, 2014. [2](#)
- [14] Sebastian Lutz, Richard Blythman, Koustav Ghosal, Matthew Moynihan, Ciaran Simms, and Aljosa Smolic. Jointformer: Single-frame lifting transformer with error prediction and refinement for 3d human pose estimation. In *2022 26th International Conference on Pattern Recognition (ICPR)*, pages 1156–1163. IEEE, 2022. [2](#), [3](#), [4](#), [6](#)
- [15] Naureen Mahmood, Nima Ghorbani, Nikolaus F Troje, Gerard Pons-Moll, and Michael J Black. Amass: Archive of motion capture as surface shapes. In *Proceedings of the IEEE/CVF international conference on computer vision*, pages 5442–5451, 2019. [2](#)
- [16] Julieta Martinez, Rayat Hossain, Javier Romero, and James J Little. A simple yet effective baseline for 3d human pose estimation. In *Proceedings of the IEEE international conference on computer vision*, pages 2640–2649, 2017. [2](#), [3](#), [6](#)
- [17] Gyeongsik Moon, Shoou-I Yu, He Wen, Takaaki Shiratori, and Kyoung Mu Lee. Interhand2.6m: A dataset and baseline for 3d interacting hand pose estimation from a single rgb image. In *Computer Vision—ECCV 2020: 16th European Conference, Glasgow, UK, August 23–28, 2020, Proceedings, Part XX 16*, pages 548–564. Springer, 2020. [2](#)
- [18] David Novotny, Nikhila Ravi, Benjamin Graham, Natalia Neverova, and Andrea Vedaldi. C3dpo: Canonical 3d pose networks for non-rigid structure from motion. In *Proceedings of the IEEE/CVF International Conference on Computer Vision*, pages 7688–7697, 2019. [1](#), [2](#), [3](#), [5](#), [6](#)
- [19] Guy Tevet, Brian Gordon, Amir Hertz, Amit H Bermano, and Daniel Cohen-Or. Motionclip: Exposing human motion generation to clip space. In *European Conference on Computer Vision*, pages 358–374. Springer, 2022. [3](#)
- [20] Guy Tevet, Sigal Raab, Brian Gordon, Yonatan Shafir, Daniel Cohen-Or, and Amit H Bermano. Human motion diffusion model. *arXiv preprint arXiv:2209.14916*, 2022. [3](#)
- [21] Ashish Vaswani, Noam Shazeer, Niki Parmar, Jakob Uszkoreit, Llion Jones, Aidan N Gomez, Łukasz Kaiser, and Illia Polosukhin. Attention is all you need. *Advances in neural information processing systems*, 30, 2017. [4](#)
- [22] Petar Veličković, Guillem Cucurull, Arantxa Casanova, Adriana Romero, Pietro Liò, and Yoshua Bengio. Graph attention networks. In *International Conference on Learning Representations*, 2018. [4](#)
- [23] Bastian Wandt, Marco Rudolph, Petrisa Zell, Helge Rhodin, and Bodo Rosenhahn. Canonpose: Self-supervised monocular 3d human pose estimation in the wild. In *Proceedings of the IEEE/CVF conference on computer vision and pattern recognition*, pages 13294–13304, 2021. [6](#)
- [24] Chaoyang Wang and Simon Lucey. Paul: Procrustean autoencoder for unsupervised lifting. In *Proceedings of the IEEE/CVF Conference on Computer Vision and Pattern Recognition*, pages 434–443, 2021. [1](#), [2](#), [3](#), [5](#)
- [25] Chaoyang Wang, Chen-Hsuan Lin, and Simon Lucey. Deep nrsfm++: Towards unsupervised 2d-3d lifting in the wild. In *2020 International Conference on 3D Vision (3DV)*, pages 12–22. IEEE, 2020. [1](#), [2](#), [4](#), [5](#)
- [26] Yu Xiang, Roozbeh Mottaghi, and Silvio Savarese. Beyond pascal: A benchmark for 3d object detection in the wild. In *IEEE winter conference on applications of computer vision*, pages 75–82. IEEE, 2014. [2](#), [5](#), [7](#)
- [27] Jiacong Xu, Yi Zhang, Jiawei Peng, Wufei Ma, Artur Jesslen, Pengliang Ji, Qixin Hu, Jiehua Zhang, Qihao Liu, Jiahao Wang, et al. Animal3d: A comprehensive dataset of 3d animal pose and shape. In *Proceedings of the IEEE/CVF International Conference on Computer Vision*, pages 9099–9109, 2023. [2](#), [7](#), [8](#)
- [28] Haitian Zeng, Xin Yu, Jiayu Miao, and Yi Yang. Mhr-net: Multiple-hypothesis reconstruction of non-rigid shapes from 2d views. In *European Conference on Computer Vision*, pages 1–17. Springer, 2022. [2](#), [5](#)
- [29] Xing Zhang, Lijun Yin, Jeffrey F Cohn, Shaun Canavan, Michael Reale, Andy Horowitz, Peng Liu, and Jeffrey M Girard. Bp4d-spontaneous: a high-resolution spontaneous 3d dynamic facial expression database. *Image and Vision Computing*, 32(10):692–706, 2014. [2](#), [7](#), [8](#)
- [30] Jianqiao Zheng, Xueqian Li, Sameera Ramasinghe, and Simon Lucey. Robust point cloud processing through posi-

tional embedding. *arXiv preprint arXiv:2309.00339*, 2023. [4](#)

- [31] Wentao Zhu, Xiaoxuan Ma, Zhaoyang Liu, Libin Liu, Wayne Wu, and Yizhou Wang. Motionbert: Unified pretraining for human motion analysis. *arXiv preprint arXiv:2210.06551*, 2022. [2](#), [4](#)
- [32] Yue Zhu, Nermin Samet, and David Picard. H3wb: Human3.6m 3d wholebody dataset and benchmark. In *Proceedings of the IEEE/CVF International Conference on Computer Vision*, pages 20166–20177, 2023. [2](#), [5](#), [6](#), [8](#), [9](#)